# Effect of zirconium doping on ZnO nanostructured thin films and the enhanced ammonia gas sensing activity

M. Sathya[1], G. Selvan[1], K. Kasirajan[2], S. Usha[2], P. Baskaran[3], and M. Karunakaran[2,*]

[1] PG and Research Department of Physics, Thanthai Hans Roever College (Autonomous), Perambalur, India
[2] Thin Film and Nanoscience Research Lab, PG and Research Department of Physics, Alagappa Government Arts College, Karaikudi 630 003, India
[3] Department of Physics, Government Arts and Science College, Veppanthattai, Perambalur, India

## ABSTRACT

A room temperature gas sensor with excellent stability and a high response has gotten a lot of interest, and there is a huge demand for them. Therefore, $NH_3$ identification is crucial for life-saving, environmental safety, and medical applications. In this research, a simple and cost-effective SILAR approach was employed to fabricate ZnO and zirconium-doped zinc oxide (Zr:ZnO) thin films on the glass substrates with varying doping concentrations. The morphologies, structures, optical, and gas sensing properties of ZnO and Zr:ZnO films are investigated. According to SEM, XRD, and Raman results confirmed that Zr is successfully incorporated on the surface of ZnO. The UV–Vis spectra suggest that films were highly transparent in the visible region with the addition of Zr content. Furthermore, the estimated optical band gap values of the Zr:ZnO thin films increased with Zr incorporation. The sensor response, sensitivity, and stability of the synthesized films were tested. Pure ZnO had a low response–recovery time of 74 s and 20 s against ammonia. Furthermore, Zr:ZnO had a faster response–recovery time of 48 s and 6 s to ammonia (3 wt.%). The Zr:ZnO films to sense 25 ppm of $NH_3$ gas at room temperature has an excellent gas response and good stability. It suggests that Zr doping improves the $NH_3$ sensing of ZnO films significantly. A framework for Zr:ZnO-based sensor sensitivity to the target gas is also suggested.

Address correspondence to E-mail: tvdkaruna@gmail.com

Ⓢ Springer

# 1 Introduction

Over the last few decades, with the fast growth of urbanization and industrialization, the devastating air pollution mainly attributed to automotive sector exhaust and factory emission has become a serious threat to human survival. With the growing need for ecological surveillance, the chemical and process management industries have drawn the attention of researchers to the tracking of highly toxic substances (e.g., $NO_2$, $NH_3$, $CO_2$, CO, and $H_2S$) in our atmosphere [1–3]. Among all the pollutants, ammonia ($NH_3$) is the most dangerous alkaline gas in the atmosphere. It is a significant nitrogen resource that contributes to the global biogeochemical nitrogen cycle and environmental change. $NH_3$ is utilized in a wide range of commercial and industrial products like ice factories, adhesives, rubber cement, automotive fuels, and laboratory chemicals. However, there is a risk of ammonia contamination in all of these applications, which can result in life-threatening exposures [4–7]. Only when the concentration of ammonia in our atmosphere reaches 50 ppm can humans detect it. Chemical factories, fertilizer plants, refrigeration systems (including cold storage facilities), drink manufacturers, and others can release ammonia into the atmosphere, causing pollution. Therefore, $NH_3$ identification is crucial for life-saving, environmental safety, and medical applications. As a result, reliable real-time gas tracking devices/sensors are key for protecting the atmosphere and humans promptly [8–10]. Many researchers are trying to create nanostructured materials to increase gas sensing efficiency relative to bulk materials. This is due to the large surface area, compact size, shape controllability, chemical composition, and physicochemical stability of nanostructured materials. As a result, low cost, high sensitivity and selectivity, environmental friendliness, and compact device designs for long-range operations are extremely crucial. For this purpose, different kinds of gas sensors have been developed such as resistive, optical, ultrasonic, and acoustic waves, thermoelectric and electrochemical ones [11–13].

Among these gas sensors, the metal–oxide–semiconductor (MOS) resistive gas sensor is one of the most prominent and has shown commendable performance in terms of sensitivity and repeatability. MOS gas sensing abilities are commonly described in terms of oxygen ionosorption, in which oxygen molecules in the atmospheric air are adsorbed to the metal oxide's surface. MOS gas sensors are commonly correlated with cost-effective production, fast response time, high sensitivity, reliable signal conversion, and significantly improved selectivity, which has resulted in comprehensive research and widespread use [14–16]. MOS gas sensors generally make use of nanosized polycrystalline n-type oxide particles, such as $WO_3$, $SnO_2$, $TiO_2$, ZnO, and $In_2O_3$, or p-type oxide particles, such as $Co_3O_4$, NiO, $Cr_2O_3$, and $Cu_2O$. This kind of gas sensor is typically used at higher temperatures [17, 18]. Heat energy is required to stimulate the adsorption of ionized oxygen species and bypass sensor response obstacles. Furthermore, the high operating temperatures might have significant disadvantages. So, one of the key challenges for this research area is to design and make reliable, stable gas sensors that are highly sensitive to target gases and can work at room temperature.

MOS gas sensors have gained a lot of exposure over the last few decades because of their unique advantages, such as low cost, high gas sensitivity, and high thermal stability. ZnO is a multi-functional semiconductor utilized in sensors, transducers, and catalysts. The gas sensing properties of ZnO have received a lot of attention in recent years. Zinc oxide is an II–VI semiconductor with many device applications. Nonetheless, zinc oxide (ZnO) has emerged as a successful and exciting contender to substitute the above-mentioned metal oxides. Because its ZnO has a significant exciton binding energy (60 meV) and a broad direct bandgap (3.37 eV) at ambient temperature. Furthermore, ZnO has a hexagonal structure and a lattice constant of $a = 0.324$–0.326 nm and $c = 0.513$–0.543 nm, making it one of the most popular and frequently used gas-sensing metal oxides [19–22]. The particle size, surface states, and oxygen adsorption all play important roles in the gas sensing function of ZnO materials. The material morphology and surface-to-volume ratio are critical parameters for improving gas sensing performance. Furthermore, metal doping is a popular approach for enhancing the gas sensing performance of ZnO thin films. As a result, by doping ZnO thin films with appropriate transition metal ions such as nickel (Ni), zirconium (Zr), manganese (Mn), copper (Cu), cadmium (Cd), cobalt (Co), and so on, the characteristics of ZnO thin films can be considerably improved [23–27]. Especially, Zr doping in ZnO has a greater

impact on its crystallite size, shape, bandgap, and sensing. Zr is an n-type impurity, and since $Zr^{4+}$ and $Zn^{2+}$ have an approximately different ionic radius of 0.74 Å and 0.84 Å, the ionic radius of $Zr^{4+}$ is larger than that of $Zn^{2+}$ [28–30]. Therefore, Zr-doped ZnO is anticipated to have improved sensing efficiency. The function of Zr dopants in the gas sensing operation is not well-established.

So many articles are reported from the literature review for the synthesis of pristine and doped ZnO films using approaches such as sol–gel, RF magnetron sputtering, SILAR, pulsed deposition, and spray pyrolysis. Among these approaches, SILAR has been received the most recognized due to its simplicity, low cost, and versatility. Furthermore, it can allow uniform mixing of elements in the precursor solution as well as a homogeneous distribution of elements (such as Zr) in the precursor solution [31, 32]. Herein, pristine and Zr-doped ZnO thin films with various Zr amounts were synthesized by the SILAR technique at room temperature. However, research on the impact of ZnO metal doping on its gas sensing operation is still very important and a challenge to explore. As a result, the current research investigated the structural, morphological, optical, and gas sensing behavior of ZnO nanostructures with varying Zr doping.

## 2 Experimental techniques

### 2.1 Chemicals

All of the compounds were analytical grade (AR) reagents that were used exactly as they were obtained, without any kind of processing. Zinc sulphate ($ZnSO_4$), sodium hydroxide (NaOH), and dopant zirconium (IV) chloride ($ZrCl_4$) were purchased from Sigma Aldrich (India). The deionized water has been utilized as a solvent during the entire manufacturing process.

### 2.2 Synthesis of Zr:ZnO films

The zirconium (Zr) doped ZnO thin films were successfully synthesized via the SILAR method with different concentrations of 1, 3, and 5 wt%. Before the deposition process, the substrate was cleaned with chromic acid and followed by acetone washing. The synthesis procedure for the modified SILAR techniques is displayed in Supp. Fig. S1. A typical synthesis process was as follows: In 50 mL ultrapure water, 0.1 M zinc sulfate and 0.2 M sodium hydroxide are dissolved and then stirred vigorously for 30 min to form a homogeneous solution ($\sim$ pH 9). A standard SILAR system has four beakers, but the reconstructed SILAR system only has two. The precursor solution is in the first beaker, while hot water is in the second. The glass substrate was vertically immersed in the sodium zincate bath for 30 s and then submerged in hot water (90 °C) for 10 s to eliminate the loosely adsorbed ions. A similar approach has been used for $\sim$ 80 dipping cycles to ensure pristine ZnO film [33]. Adding different amounts of zirconium chloride as Zr source (i.e. 1, 3, and 5 wt.%) in the sodium zincate bath during the doping process. Eventually, the coated films were dried in the air and annealed for 2 h at 400 °C to produce Zr:ZnO films.

### 2.3 Characterization

Table 1 represents a concise description of the characterization techniques.

### 2.4 Gas sensing measurement

The construction of the homemade sensing setup is schematically displayed in Supp. Fig. S2. The $NH_3$ arrives from an available commercially ammonium hydroxide solution. During gas response evaluations, the conductive silver paste was used to establish ohmic contact on the surface of the thin films. The electrical contacts are connected to the desktop interlinked with high resistance electrometer (Keithley electrometer 6514, USA). The gas chamber was self-designed and linked to a Keithley electrometer, gas flow meters, and the tube furnace. From the gas sensing setup, the resistance changes when exposed to air ($R_a$) and $NH_3$ gas ($R_g$). The appropriate amount (ppm) of $NH_3$ was then injected into the tube using the chromatographic syringe. The ammonia solution is then heated in the sensing chamber to create $NH_3$ vapor. Then, suddenly a shift of resistance concerning the baseline was observed. The sensor response, response–recovery time, and stability of the Zr:ZnO films are done at 25 ppm of $NH_3$ gas.

**Table 1** Characterization techniques for synthesized Zr:ZnO thin films

| S.No | Techniques | Instrument name | Parameters |
|---|---|---|---|
| 1 | X-ray diffraction pattern | X-Pert PRO X-ray diffractometer | Crystal phase and crystallinity |
| 2 | Scanning electron microscope | JEOL JSM 5800 LV | Morphology, size, and roughness |
| 3 | Energy dispersive spectrum | EDX system (SU-70, Hitachi) | Chemical composition and purity |
| 4 | Elemental mapping analysis | XL G2 Desktop Scanning Electron Microscope | Uniform element distributions |
| 5 | UV–Vis spectroscopy | UV–Vis, JMNU-3010 | Identification of the compounds |
| 6 | PL spectroscopy | Oxford low temperature LN2 77 K set up | The crystalline quality of materials |
| 7 | Raman spectroscopy | STR 500 mm Laser Raman spectrometer | Vibrational modes of molecules |

# 3 Result and discussion

## 3.1 Scanning electron microscope and EDS analysis

The scanning electron microscope (SEM) is an interesting technique for determining sample morphology, and it provides important information on the shape and size of the synthesized thin films. The surface morphology of ZnO and Zr:ZnO thin solid films deposited from the glass substrate with various amounts (1%, 3%, and 5%) is displayed in Fig. 1a–d. It is observed that the undoped ZnO thin film exhibits nano-flower surface morphology is displayed in Fig. 1a. The images demonstrate that increasing the Zr concentration changes the surface morphology of the films. The increasing Zr amount in the solution ascertains that the surface becomes slightly smooth and the grain size reduces. The morphology was modified into a flower shape after Zr doping, and rods were distributed over the flowers as a secondary grain, as shown in Fig. 1b, c. These observations are following the XRD tests, which show that as the Zr concentration increases, the grain size of the film decreases. These neighbouring nanoflowers and nanorods are interconnected, which allowing gas to migrate into the material's inner space and so increasing NH$_3$ vapor sensing.

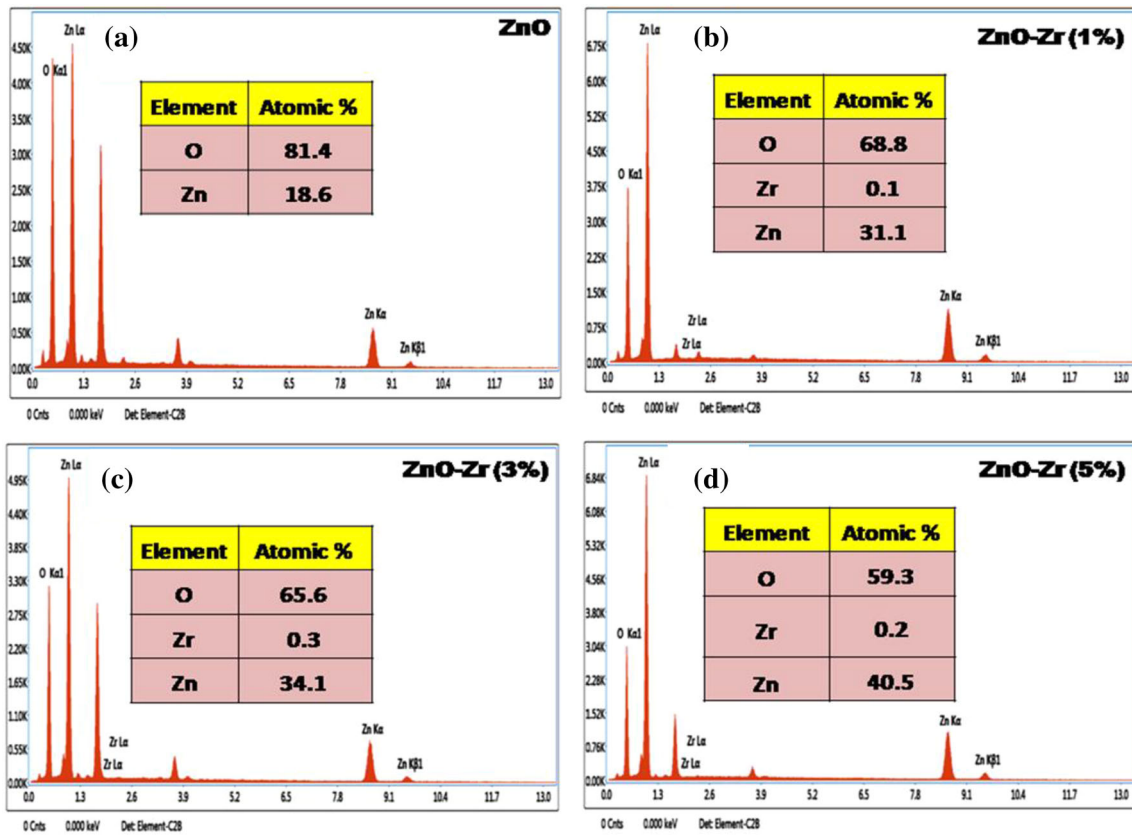**Fig. 1 a–d** SEM images of the prepared ZnO and different wt.% of Zr:ZnO thin films
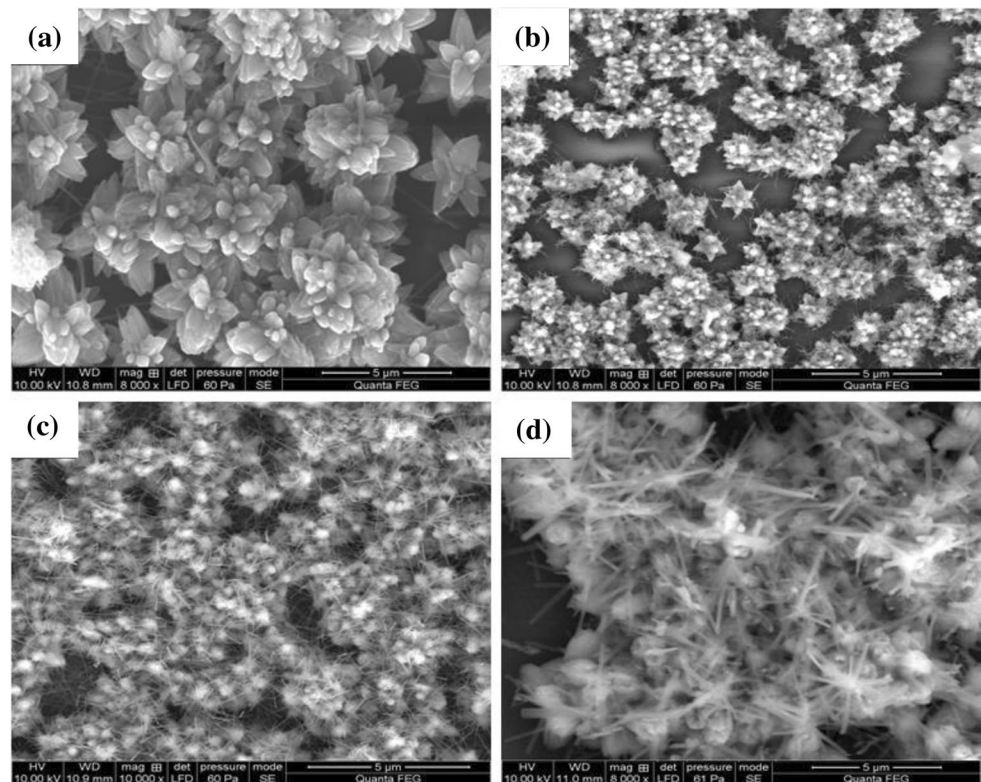
Fig. 2 a–d EDS spectrum of ZnO and different wt.% of Zr:ZnO thin films

The chemical composition of ZnO thin films synthesized using SILAR deposition was analyzed by EDS spectrum. Figure 2a–d displays the EDS spectra of films deposited at different Zr doping concentrations ranging from 0 to 5%. The EDS spectrum reveals the existence of zinc (Zn) and oxygen (O) in the pristine ZnO material is displayed in Fig. 2a. Furthermore, the EDS spectrum reveals the (Zn), (O), and zirconium (Zr) are present in the Zr:ZnO material as displayed in Fig. 2b–d. Furthermore, the findings demonstrate that there are no additional contaminants in the synthesized films. The elemental mapping images of the Zr:ZnO (3%) thin films are displayed in Fig. 3a–d, with all scale bars set to 30 μm. Figure 3a shows the overall elemental mapping for the Zr:ZnO films, which indicates a uniform distribution of the Zn element (red), O (green), and Zr (blue).

## 3.2 Crystallography investigation

The XRD pattern of ZnO and Zr-doped ZnO thin films coated on micro-glass substrates for various doping concentrations is displayed in Fig. 4. It can be seen that all the films are polycrystalline with a hexagonal wurtzite-type structure. All Braggs reflections were found at $2\theta = 31°$, $34°$, $36°$, $47°$, $56°$, $63°$, $67°$, and $69°$ is relating to the (100), (002), (101), (102), (110), (103), (112), and (201) planes of pristine ZnO (JCPDS Card-No. 36-1451) [34]. No other impurities are detected in the ZnO films. Furthermore, the disappearance of Zr and $ZrO_2$-related peaks in the XRD pattern suggests pure ZnO formation. In comparison to the standard sequence, the undoped film revealed a preference for the (002) direction is high and a lack of growth in the (100), (101), (102), (110), (103), (112), and (201) directions. Generally, ZnO films have a high-intensity peak for the (002) plane, suggesting that the plane has low surface energy. After doping to 1, 3 wt% with Zr, the XRD pattern indicated a preferential orientation in the (101) region, with other planes (100) and (002) are suppressed. In contrast, the

**Fig. 3** The elemental mapping images of the Zr:ZnO (3%) thin films
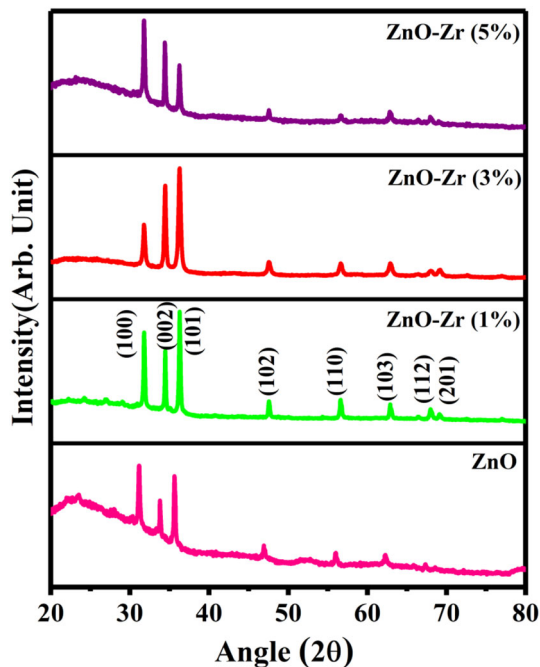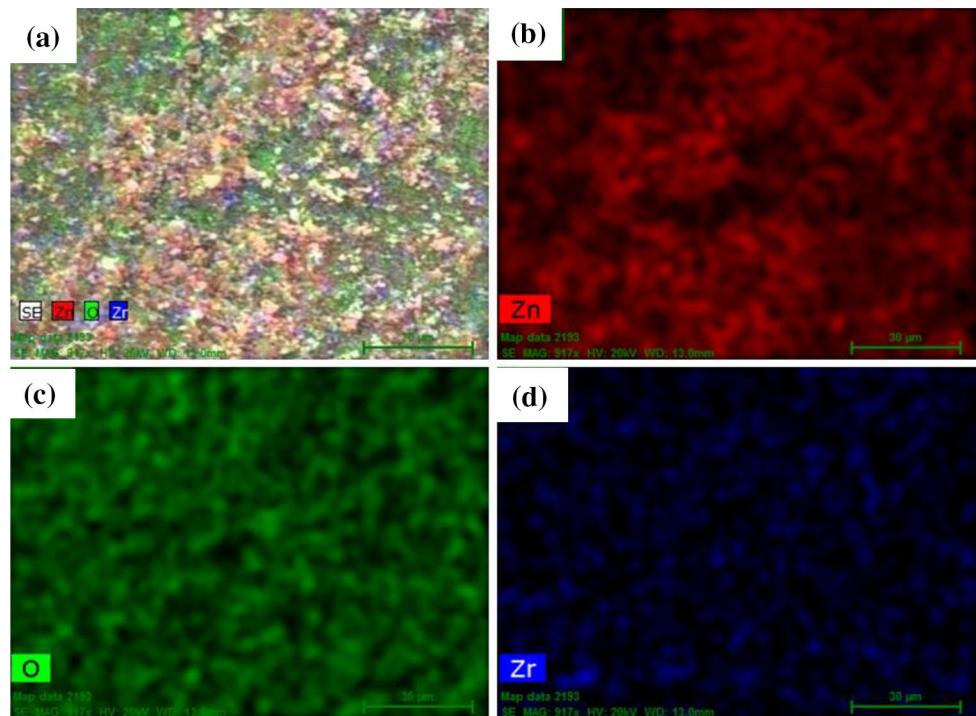




Fig. 4 X-ray diffraction patterns of ZnO and Zr:ZnO films with different Zr-doping concentrations

peak (100) becomes extremely dominant when the doping concentration of Zr is high (wt. 5%). Another intriguing finding is peak change and broadening about doped samples as compared to undoped ZnO. Peak adjustments toward the upper and lower planes

in doped samples mean that $Zr^{4+}$ ions with greater ionic radii ($\sim$ 0.84 Å) have been replaced by dopant ions with smaller ionic radii (Zn $\sim$ 0.74 Å). The microstructural parameters of lattice constant, crystallite size, dislocation density, strain, and number of crystallite values are noted in Table 2. The average crystallite size was estimated depending on the preferential orientation of the planes using Debye–Scherrer's formula [35]

$$D = \frac{0.9\lambda}{\beta cos\theta} \tag{1}$$

where $\theta$ is the Bragg's angle, $\beta$ is the the full width at half maximum of the diffraction line, $\lambda$ is the the wavelength of the X-ray radiation (which is assumed to be 0.154 nm), and $k$ is the denotes the shape factor (which is assumed to be 0.9). According to the above relationships, the estimated crystalline size of the undoped ZnO films is 46 nm, while the Zr:ZnO (1–5 wt%) films are 45, 25, and 34 nm, respectively. When the doping concentration of Zr increases, the average crystalline size initially increases and then decreases. The reduction of size is primarily caused by foreign contaminants distorting the host ZnO lattice. The other parameters like dislocation density ($\delta$), strain ($\varepsilon$), and number of crystallites ($N$) of the Zr:ZnO films have been estimated by using the relations [36]

**Table 2** The estimated values of crystalline size, strain, dislocation density and, lattice constants for ZnO and Zr:ZnO thin films

| Zr concentration (wt%) | Lattice constants (Å) | | Film thickness (nm) | Crystallite size (nm) | Dislocation density ($\times 10^{15}$) lines m$^{-2}$ | Strain ($\times 10^{-3}$) | Number of crystallites ($\times 10^{16}$ m$^{-2}$) | Band gap (eV) |
|---|---|---|---|---|---|---|---|---|
| | $a$ | $c$ | | | | | | |
| 0 | 2.86032 | 4.95422 | 940 | 46 | 0.4829 | 2.45 | 0.997 | 3.00 |
| 1 | 2.85823 | 4.95061 | 850 | 45 | 0.4870 | 2.46 | 0.913 | 3.10 |
| 3 | 2.85979 | 4.95330 | 760 | 25 | 1.5915 | 4.45 | 4.825 | 3.25 |
| 5 | 2.86075 | 4.95496 | 800 | 34 | 0.8912 | 3.78 | 2.128 | 3.15 |

$$\delta = \frac{1}{D^2} \tag{2}$$

$$\epsilon = \frac{\beta \cot \theta}{4} \tag{3}$$

$$N = \frac{t}{D^3} \tag{4}$$

It is observed that the dislocation density, strains, and the number of crystallites gradually increase and then decrease with the increase of the Zr concentration. As a result, Zr doping generates more nucleation sites, leading to the formation of smaller crystallite sizes. The lattice constants '$a$' and '$c$,' as well as the unit cell volume '$V$,' are calculated from XRD using the following relationships.

$$V = a^2 c (\sin 60°) \tag{5}$$

$$\frac{1}{d^2} = \frac{4}{3} \left\{ \frac{h^2 + hk + k^2}{a^2} \right\} \left\{ \frac{l^2}{c^2} \right\} \tag{6}$$

The evaluated lattice constants '$a$' and '$c$' and unit cell volume '$V$' for Zr:ZnO films indicated that the cell volume and both '$a$' and '$c$' parameters have been decreased with increasing Zr doping.

### 3.3 Raman analysis

The Raman spectrum is used to assess the crystal quality, structural defects, and vibrational modes in a synthesized film. The Raman spectrum of ZnO and Zr:ZnO thin films coated from the glass substrate with various amounts (1%, 3%, and 5%) is displayed in Fig. 5. In Raman scattering the B$_1$ modes are silent, while the A$_1$ and E$_1$ modes are polar and hence show distinct vibrations for the transverse optical (TO) and longitudinal-optical (LO) phonons. Non-polar E$_2$ phases contain two different wavelengths, $E_2^{high}$ and $E_2^{low}$, which are correlated to the mobility of

oxygen atoms and zinc sublattice, respectively. The Raman spectra display different vibrational modes observed at 338 cm$^{-1}$, 382 cm$^{-1}$, 436 cm$^{-1}$, 476 cm$^{-1}$ and 570 cm$^{-1}$ [37]. The broad Raman peak at 338 cm$^{-1}$ is attributed to the $E_2^{high} - E_2^{low}$ multiple-phonon scattering process and A$_1$T as phonon with A$_1$ symmetry for transverse optical frequency mode are detected at 382 cm$^{-1}$. The sharp and predominant peak mode was detected at 436 cm$^{-1}$ which was assigned as $E_2^{high}$ mode illustrating the band signature of the hexagonal wurtzite crystal structure of ZnO films. Furthermore, the most intense $E_2^{high}$ vibrational mode suggests the wurtzite structure with good crystallinity in the films, which is consistent with XRD findings. The other at band 570 cm$^{-1}$ is allocated to A$_1$ (LO) mode. Careful inspection suggests that the addition of zirconium atoms influenced the vibrational characteristic and crystallographic structure of the ZnO films [38, 39]. The incorporation of the dopant reduced the peak intensity to $\sim$ 432 cm$^{-1}$. This local vibration may be caused by the
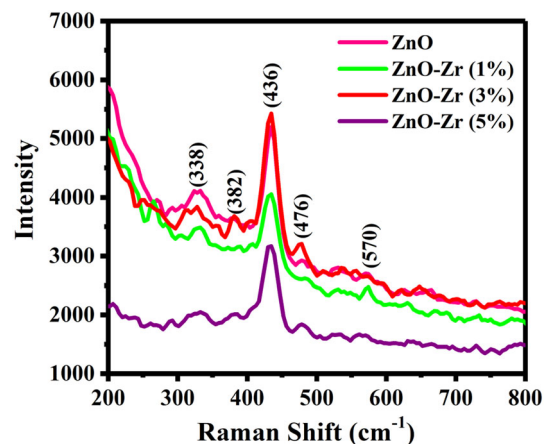


**Fig. 5** Raman spectra of coated Zr:ZnO films with various amounts of Zr−doping

replacement of certain Zn atoms with Zr in the ZnO lattice structure.

## 3.4 UV–Vis spectroscopy

The optical characteristics such as transmittance, absorption coefficient, and bandgap are significant because they govern the properties of a material in numerous applications. The optical transmission spectra of synthesized ZnO and Zr:ZnO thin film with different doping concentrations of the samples have been evaluated using a UV–Vis spectrophotometer at a wavelength range of 200–800 nm is displayed in Fig. 6a. As seen in Fig. 6a, the observed that undoped ZnO film has low transparency, and notably over 450 nm wavelength. The optical transmittance initially increases and then decreases in the visible region depending on the increase of Zr concentration. The films are highly transparent in the visible range, with a mean optical transmittance
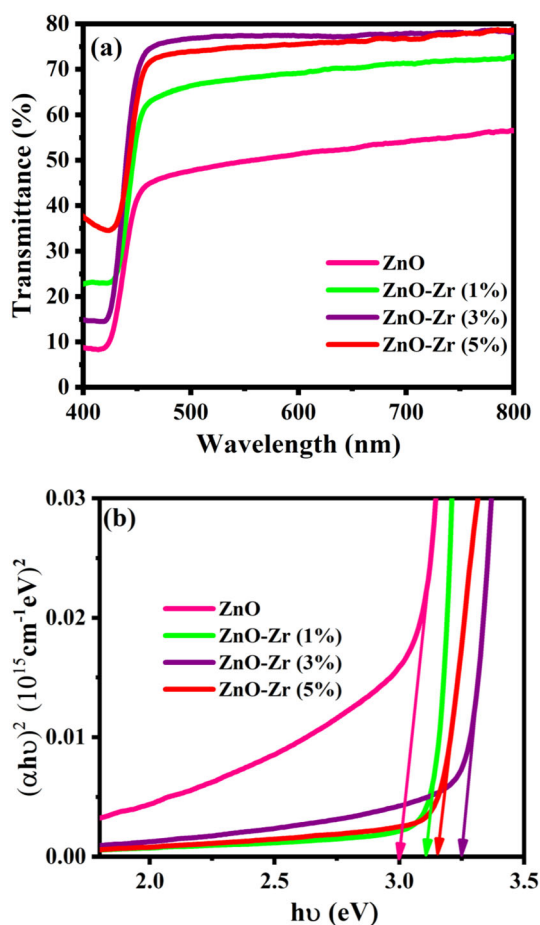


varying from 40 to 75%. At 5 wt% Zr-doped ZnO films saw a small drop in average transmittance from 75 to 70%. The maximum transmittance of 75% is found for the Zr:ZnO (3%) thin films. A significantly higher transmittance rate for doped ZnO thin films may be due to the most crystalline aspect of the film. The absorption coefficient of the thin films depends on the energy of the incident photon. The optical band gap (Eg) films were evaluated using the Tauc Equations [40],

$$(\alpha h\vartheta)^2 = A(h\vartheta - E_g) \tag{7}$$

where $E_g$ is the optical band gap, $h\upsilon$ is the incident photon energy, $A$ is a proportionality constant, and $\alpha$ is the absorption coefficient. Tauc's plot approach, seen in Fig. 6b, involves plotting $(\alpha h\upsilon)^2$ against $h\upsilon$ and extrapolating the linear portion of the absorption edge to the energy axis (straight line portion). The bandgap energy of the related samples is predicted to be 3.0, 3.10, 3.25, and 3.15 eV for ZnO, and Zr:ZnO (1–5%), respectively. In this scenario, the calculated band gap value of Zr:ZnO thin film (3.25 eV) is slightly greater than the bandgap value of undoped ZnO thin film (3.0 eV). Because of the change of peak shift in the transmittance curve and the quantum size effect, the measured band gap value is initially increased and subsequently sharply decreased with increasing Zr-doping concentration. Furthermore, the change of the bandgap is primarily determined by the surface structure of the film.

## 3.5 Photoluminescence investigations

Photoluminescence (PL) spectroscopy is a non-destructive light assessment approach that can track the presence of defects in samples. The PL spectra of synthesized ZnO and Zr:ZnO (1–5%) thin film with different doping concentrations of the samples have been evaluated are displayed in Fig. 7. In the PL spectra, the three emission peaks are noticeable: one is the band edge peak, and the other two are intertwined to defect rates like zinc (interstitial, vacancy), oxygen (interstitial, vacancy). The UV emission peak (385 nm) is due to the recombination of electrons and holes. In the visible area, the peak position at 412 nm, which is a near band edge (NBE) emission, has a lower intensity [7]. The location of NBE emission illustrates the consecutive blue movement for (1–5%) Zr:ZnO. The sharp and dominant emission bands found in the spectra at 489 nm are attributed to the
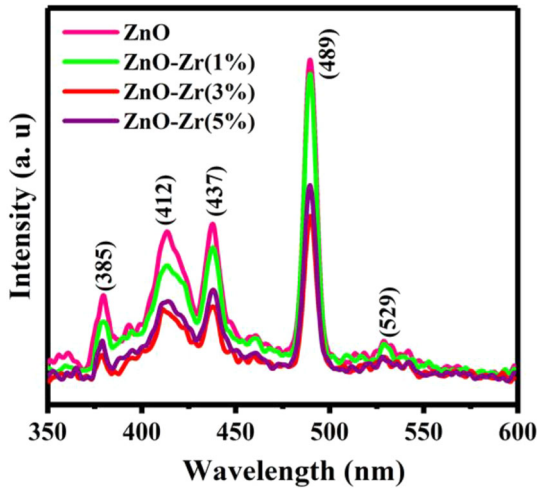
**Fig. 6 a** Transmittance spectra of ZnO and Zr:ZnO thin films and **b** optical band gap values of ZnO and Zr:ZnO thin films

**Fig. 7** Photoluminescence spectrum of ZnO and different wt% of Zr:ZnO thin films

electronic transition possibility from the donor level of zinc interstitial ($Zn_i$) to the acceptor level of zinc vacancy ($V_{Zn}$), as the co-existence of these two defects is quite probable. The peak located at 529 nm is contributed to the oxygen vacancies. The intensity and position of this PL emission are also affected by Zr doping [41, 42]. This emission peak has moved significantly to the lower wavelength region as a result of the addition of Zr. The optical band gap expands as the number of free electrons in a semiconductor system rises, according to the Moss–Burstein effect.

## 3.6 Gas sensitivity investigations

The process of gas detection is essentially a surface phenomenon. The adsorption/desorption of gases, as well as the surface reaction with adsorbed oxygen, are highly beneficial for generating an exceptional gas sensor. The Zr:ZnO thin film was synthesized using the SILAR approach at different doping concentrations for the gas sensing properties. The Zr:ZnO-based metal oxide semiconductor was exposed with ammonia gas vapors at various concentrations. The response of the 3 wt% Zr:ZnO thin film for (25 ppm to 125 ppm) $NH_3$ concentration at room temperature is displayed in Fig. 8a. The rate of resistance changes concerning time for particular target gas can be expressed as the following relation:

$$S = \frac{R_a}{R_g} \tag{8}$$

where $R_a$ and $R_g$ are the electrical resistance of the thin film measured in the target air and target gas. It has been noted that with a rise in $NH_3$ gas concentration and the gas response (%) is also raised. Figure 8b illustrated the measured responses and recovery time of ZnO thin films with $NH_3$ gas at a concentration of 25 ppm. The pristine ZnO film has a response–recovery time of 74 s and 20 s. The response time ($T_{res}$) is the time it takes for the sensor to reach 90% of total resistance (adsorbed gas time), and the recovery time is the time it takes for the sensor to re-achieve 90% of total resistance (desorbed gas time) ($T_{rec}$). The 3D cylinder diagram illustrates
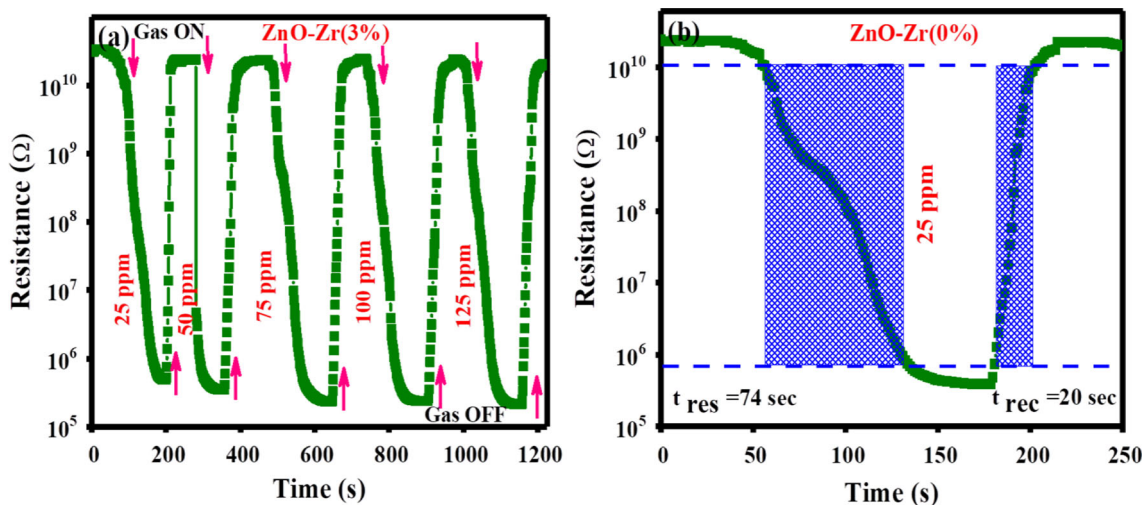


**Fig. 8** **a** Gas response of Zr:ZnO (wt. 3%) films deposited on a glass substrate with exposure and removal of $NH_3$ gas with concentrations of 25 ppm to 125 ppm at room temperature and **b** response time ($t_{res}$) and recovery time ($t_{rec}$) of ZnO thin film
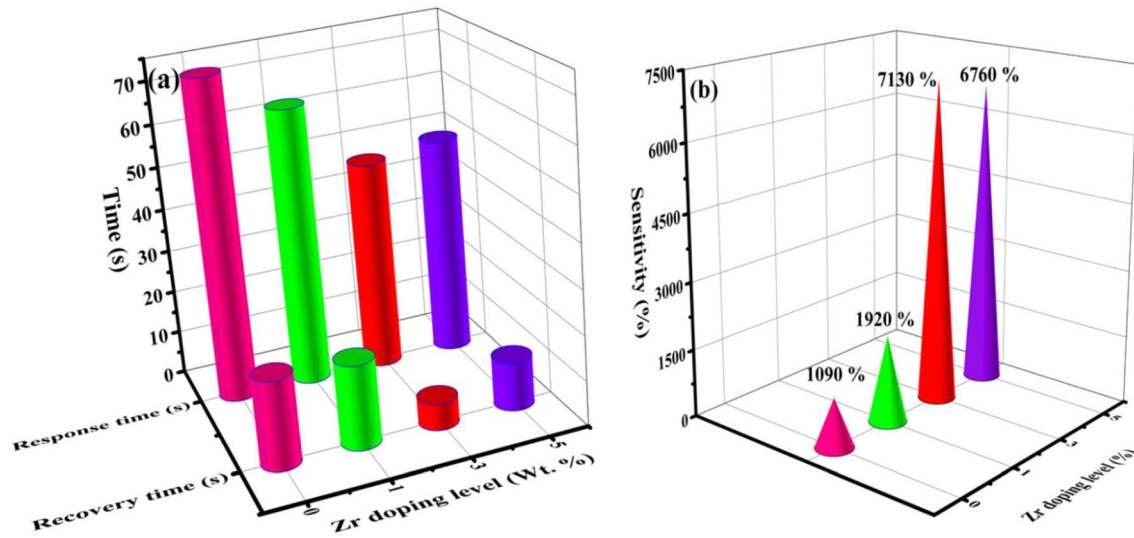
**Fig. 9 a** 3D cylinder diagram shows the response time ($t_{res}$) and recovery time ($t_{rec}$) of ZnO and Zr:ZnO thin films with various Zr-doping concentrations and **b** 3D cone diagram shows the sensitivity towards various concentrations of Zr:ZnO thin films

**Table 3** Response, recovery time and sensitivity of different wt.% of Zr:ZnO thin films for 25 ppm $NH_3$

| Zr concentration (wt.%) | Response time (s) | Recovery time (s) | Sensitivity (%) |
|---|---|---|---|
| 0 | 74 | 20 | 1090 |
| 1 | 64 | 19 | 1920 |
| 3 | 48 | 6 | 7130 |
| 5 | 50 | 11 | 6760 |

the response–recovery behavior of ZnO and Zr:ZnO (1 wt.%, 3 wt.% and, 5 wt.%) sensors at 25 ppm of $NH_3$ gas at their room temperature is displayed in Fig. 9a. As the sensors were exposed to $NH_3$ gas, their resistance values are reduced. The resistance recovered to its initial value when the $NH_3$ gas was exchanged with air. This resistance shift was noted throughout all sensors. Table 3 displayed the estimated response–recovery time for the various Zr doping concentrations. The response–recovery time reduces as the amount of Zr doping rises. In contrast to other films, the 3 wt% Zr:ZnO film has a quick response (48 s) and recovery (6 s) time. The sensitivity activity of the manufactured sensors was examined by exposing them to $NH_3$ vapors at different doping concentrations, as shown in Fig. 9b. The observed sensitivity value for the various Zr doping concentrations is displayed in Table 3. The sensing response increases with Zr content and achieves a maximum at 3 wt.% Zr content while decreasing in 5 wt.% Zr-doped ZnO films. As compared to pure ZnO film, the increased Zr content exhibits a better response to $NH_3$ gases. As a result,

the sensor based on Zr:ZnO (3 wt.%) film demonstrated improved sensitivity to $NH_3$ gas. A comparison of the sensing performance of ZnO and various metal-doped ZnO with other $NH_3$ sensors reported in the literature is provided in Table 4.

### 3.7 Stability of the Zr:ZnO sensor

The collection of long-term stability of undoped and rare-earth-doped ZnO sensors was stored in the desiccator. The stability of the ZnO and Zr:ZnO films were examined, and the results are shown in Fig. 10. At a time interval of 15 days, one strip was removed and then exposed to only a fixed concentration (25 ppm) of $NH_3$ gas in the test chamber. The sensitivity of the sensor was estimated at room temperature. This has been extended over 60 days. The pristine ZnO, and (1 wt.%, 5 wt.%) sensors showed limited stability with low response during operation. The Zr:ZnO (3 wt%) sensors showed excellent stability with a response of more than 7000% drift during its two months of operation. A good shelf-life and the

**Table 4** A comparison of the sensing performance of ZnO and various metal doped ZnO with other $NH_3$ sensors reported in literature

| S. no. | Material | Method | Operating temperature (°C) | Concentration (ppm) | Response time (s) | Recovery time (s) | References |
|--------|----------|--------|----------------------------|---------------------|-------------------|-------------------|------------|
| 1 | ZnO | Nebulizer spray pyrolysis | 400 | 100 | 120 | 10 | [43] |
| 2 | ZnO:Ba | Nebulizer spray pyrolysis | 250 | 600 | 130 | 40 | [44] |
| 3 | ZnO:Cr | Nebulizer spray pyrolysis | RT | 200 | 67 | 13 | [45] |
| 4 | Mg:ZnO | SILAR | RT | 100 | 25 | 6 | [46] |
| 5 | W:ZnO | Perfume spray pyrolysis | RT | 100 | 293 | 13 | [47] |
| 6 | ZnO:Pd | Chemical precipitation | 350 | 40 | 21 | 79 | [48] |
| 7 | Zr:ZnO | SILAR | RT | 25 | 48 | 6 | Present work |
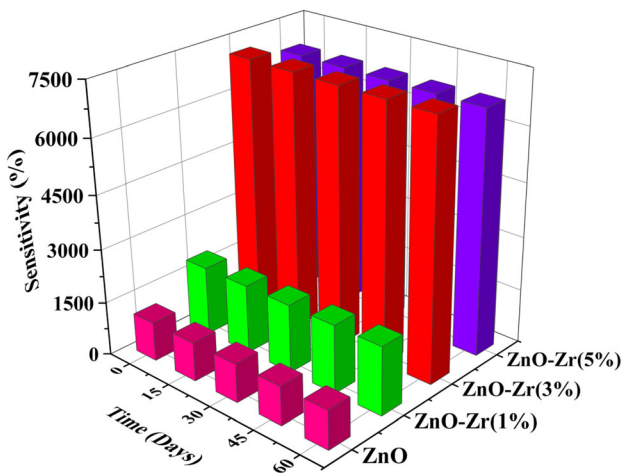


**Fig. 10** Stability towards various loading amounts of Zr:ZnO thin films at 25 ppm concentrations

almost constant sensing efficiency of the sensor indicate that the Zr:ZnO (3 wt.%) sensor qualifies at room temperature as a reliable $NH_3$ gas sensor.

## 3.8 Gas sensing mechanism

Gas sensing pathways illustrate that gas can induce changes in a sensor's electrical properties. We assume that the most commonly used gas sensing systems can be classified into two types. One group includes concepts such as Fermi level control theory and grain boundary barrier control theory, which describe improvements in electrical properties from a comparatively microscopic context. The other kind of theory is relatively macroscopic, with a primary emphasis on the interaction of materials and gases.

This type of theory includes the adsorption/desorption model, the bulk resistance control mechanism, and the gas diffusion control mechanism. The gas sensing mechanism of these chemical-resistance sensors is directly related to the electron exchange created by the oxidation-reduction reaction between the material's surface electrons and the target gas. The gas adoption mechanism of the pristine ZnO and Zr:ZnO (3 wt.%) gas sensor in the $NH_3$ gas atmosphere at room temperature is displayed in Fig. 11. In general, it can be described as follows: the development of chemisorbed oxygen species ($O_2^-$) or atomic ($O^-$, $O^{2-}$) on the sensor surface is caused by trapping electrons in the conduction band and controlling their movement which creates the electron depletion region. Eventually, an increase in electrical resistance was observed. The following equation helps to describe this process [49]:

$$O_{2(gas)} \rightarrow O_{2(ads)} \tag{9}$$

$$O_{2(ads)} + e^- \rightarrow O_{2(ads)}^- \tag{10}$$

$$O_{2(ads)}^- + e^- \rightarrow 2O_{(ads)}^- \tag{11}$$

$$2O_{(ads)}^- + e^- \rightarrow O_{(ads)}^{2-} \tag{12}$$

When exposed to $NH_3$, the $NH_3$ gas interacts with the adsorbed oxygen ions, releasing the trapped electron and resulting in a narrower space charge and a reduced barrier potential. As a result, the resistance in the gas sensor reduces. This phenomenon can be discussed as follows [50]
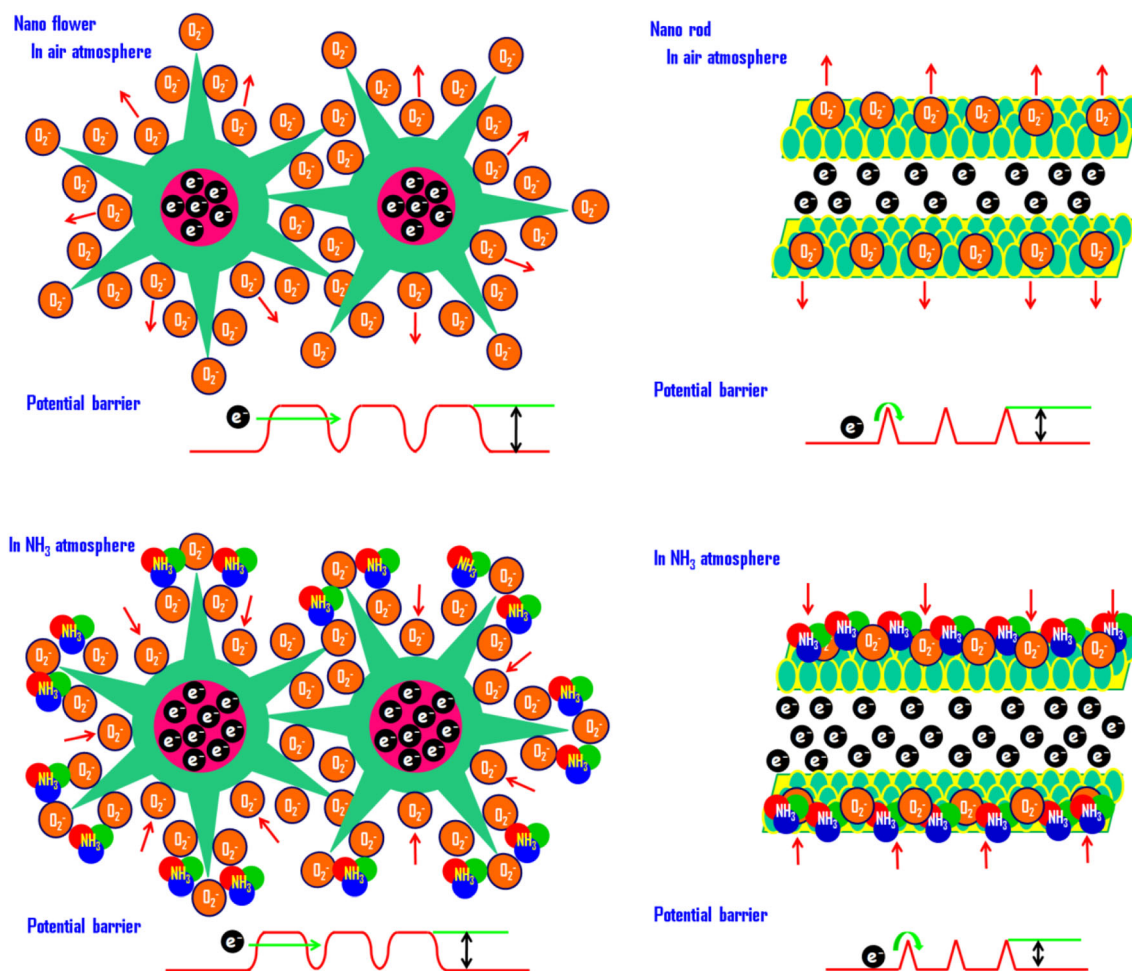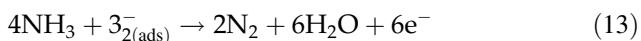
**Fig. 11** Gas sensing mechanism of the ZnO and Zr:ZnO thin films gas sensor in the NH$_3$ gas atmosphere

$$4NH_3 + 3_{2(ads)}^- \rightarrow 2N_2 + 6H_2O + 6e^- \qquad (13)$$

The introduction of NH$_3$ (reducing gas) near the surface of the ZnO thin film triggers an electron exchange between the NH$_3$ and the charged oxygen ions (adsorbed), allowing the captivated electrons to move to the conduction band. This approach reduces the thickness of the depletion layer, due to its reduction in the resistance of the sensor. The Zr:ZnO (3 wt.%) network will increase the surface area of the sensing film, creating the ability of gas molecules to adsorption and desorption. Therefore, nanorod surface and high electron carrier concentration can be contributed to the significant increase in the NH$_3$ sensitivity of the doped films.

## 4  Conclusions

In summary, ZnO and Zr-doped ZnO thin films were successfully synthesized using the SILAR approach with varying amounts from 1 to 5 wt.%. The synthesized films are investigated by different characterization techniques. The SEM pictures suggested the conversion of flower-like morphology into flower-like nanorod interconnected topology (3 wt.%) upon the insertion of Zr in the ZnO. The XRD pattern suggests that raising the Zr concentration causes the peaks to expand, indicating a decrease in crystallite size with doping. The optical transmittance is increased in the visible region depending on the increase of Zr concentration and the optical bandgap values are ∼ 3.0–3.25 eV for ZnO and Zr:ZnO (1–5 wt.%). The Zr:ZnO (3 wt.%) film sensor based on this flower-like nanorod structure detects the NH$_3$ vapors with a rapid response and high sensitivity at room

temperature. So, the Zr:ZnO (3 wt.%) sensor has a fast response–recovery time of 48 s and 6 s towards the 25 ppm of $NH_3$ gas. The Zr:ZnO sensor demonstrated excellent stability and repeatability when exposed to ammonia gas for 60 days at a dose of 25 ppm. So, These findings established reliable and cost-effective conductometric Zr:ZnO sensor has promising applications in the field of low concentration ammonia gas detection.

**Supplementary Information:** The online version contains supplementary material available at http s://doi.org/10.1007/s10854-021-07318-y.

# References

1. S.B. Vijendra, M.K. MirabbosHojamberdiev, Enhanced sensing performance of ZnO nanostructures-based gas sensors: a review. Energy Rep. **6**, 46–62 (2020). https://doi.org/10.1016/j.egyr.2019.08.070

2. I. Manisalidis, E. Stavropoulou, A. Stavropoulos, E. Bezirt-zoglou, Environmental and health impacts of air pollution: a review. Front. Public Health **8**, 14 (2020). https://doi.org/10.3389/fpubh.2020.00014

3. Z. Li, H. Li, Z. Wu, M. Wang, J. Luo, H. Torun, P.A. Hu et al., Advances in designs and mechanisms of semiconducting metal oxide nanostructures for high-precision gas sensors operated at room temperature. Mater. Horiz. **6**(3), 470–506 (2019). https://doi.org/10.1039/C8MH01365A

4. Tu. Ying, C. Kyle, D.-W. HuiLuo, A. Das, J. Briscoe, S. Dunn, M.-M. Titirici, S. Krause, Ammonia gas sensor response of a vertical zinc oxide nanorod-gold junction diode at room temperature. ACS Sens. **5**(11), 3568–3575 (2020). https://doi.org/10.1021/acssensors.0c01769

5. R. Kumar, X. Liu, J. Zhang, M. Kumar, Room-temperature gas sensors under photoactivation: from metal oxides to 2d materials. Nano-Micro Lett. **12**(1), 1–37 (2020). https://doi.org/10.1007/s40820-020-00503-4

6. Y. Seekaew, W. Pon-On, C. Wongchoosuk, Ultrahigh selective room-temperature ammonia gas sensor based on tin–titanium dioxide/reduced graphene/carbon nanotube nanocomposites by the solvothermal method. ACS Omega **4**(16), 16916–16924 (2019). https://doi.org/10.1021/acsomega.9b02185

7. J. Santhosam, K. Ravichandran, M. Shkir, M. Sridharan, Effect of La incorporation on the $NH_3$ sensing behaviour of ZnO thin films prepared using low-cost nebulizer spray technique. J Mater. Sci: Mater. Electron. **31**(16),

8. A. Kumar, A. Sanger, A. Kumar, R. Chandra, Fast response ammonia sensors based on $TiO_2$ and NiO nanostructured bilayer thin films. RSC Adv. **6**(81), 77636–77643 (2016). https://doi.org/10.1039/C6RA14342C

9. V.N. Narwade, S.R. Anjum, V. Kokol, R.S. Khairnar, Ammonia-sensing ability of differently structured hydroxyapatite blended cellulose nanofibril composite films. Cellulose **26**(5), 3325–3337 (2019). https://doi.org/10.1007/s10570-019-02299-y

10. B. Chatterjee, A. Bandyopadhyay, Development of zinc oxide sensors for detecting ammonia gas in the ambient air: a critical short review. Manage. Environ. Qual. **26**(1), 89–105 (2016). https://doi.org/10.1002/tqem.21483

11. L. Zhu, W. Zeng, Room-temperature gas sensing of ZnO-based gas sensor: a review. Sens. Actuators A Phys. **267**, 242–261 (2017). https://doi.org/10.1016/j.sna.2017.10.021

12. G. Manjunath, P. Nagaraju, S. Mandal, A comparative study on enhancer and inhibitor of glycine–nitrate combustion ZnO screen-printed sensor: detection of low concentration ammonia at room temperature. J. Mater. Sci. Mater. Electron. **31**, 10366–10380 (2020). https://doi.org/10.1007/s10854-020-03584-4

13. K. Haddad, A. Abokifa, S. Kavadiya, B. Lee, S. Banerjee, B. Raman, P. Banerjee, C. Lo, J. Fortner, P. Biswas, $SnO_2$ nanostructured thin films for room-temperature gas sensing of volatile organic compounds. ACS Appl. Mater. Interfaces **10**(35), 29972–29981 (2018). https://doi.org/10.1021/acsami.8b08397

14. D. Degler, U. Weimar, N. Barsan, Current understanding of the fundamental mechanisms of doped and loaded semiconducting metal-oxide-based gas sensing materials. ACS Sens. **4**(9), 2228–2249 (2019). https://doi.org/10.1021/acssensors.9b00975

15. Y. Chen, M. Li, W. Yan, X. Zhuang, K.W. Ng, X. Cheng, Sensitive and low-power metal oxide gas sensors with a low-cost microelectromechanical heater. ACS Omega **6**(2), 1216–1222 (2021). https://doi.org/10.1021/acsomega.0c04340

16. W. Guan, N. Tang, K. He, X. Hu, M. Li, K. Li, Gas-sensing performances of metal oxide nanostructures for detecting dissolved gases: a mini review. Front. Chem. **8**, 76 (2020). https://doi.org/10.3389/fchem.2020.00076

17. P. Nakarungsee, S. Srirattanapibul, C. Issro, I.-M. Tang, S. Thongmee, High performance Cr doped ZnO by UV for $NH_3$ gas sensor. Sens. Actuators A Phys. **314**, 112230 (2020). https://doi.org/10.1016/j.sna.2020.112230

18. X.Q. Zheng, H.Y. Cheng, Flexible and stretchable metal oxide gas sensors for healthcare. Sci. China Technol. Sci.

**62**(2), 209–223 (2019). https://doi.org/10.1007/s11431-018-9397-5

19. S. Wang, F. Jia, X. Wang, L. Hu, Y. Sun, G. Yin, T. Zhou, Z. Feng, P. Kumar, B. Liu, Fabrication of ZnO nanoparticles modified by uniformly dispersed Ag nanoparticles: enhancement of gas sensing performance. ACS Omega **5**(10), 5209–5218 (2020). https://doi.org/10.1021/acsomega.9b04243

20. X. Li, X. Zhu, K. Jin, Study on structural and optical properties of Mn-doped ZnO thin films by sol-gel method. Opt. Mater. **100**, 109657 (2020). https://doi.org/10.1016/j.optmat.2020.109657

21. Y.-T. Tsai, S.-J. Chang, L.-W. Ji, Y.-J. Hsiao, I.-T. Tang, H.-Y. Lu, Y.-L. Chu, High sensitivity of NO gas sensors based on novel Ag-doped ZnO nanoflowers enhanced with a UV light-emitting diode. ACS Omega **3**(10), 13798–13807 (2018). https://doi.org/10.1021/acsomega.8b01882

22. Z.N. Kayani, B. Amir, S. Riaz, S. Naseem, Antibacterial, magnetic, optical and dielectric analysis of novel $La_2O_3$ doped ZnO thin films. Opt. Mater. **109**, 110287 (2020). https://doi.org/10.1016/j.optmat.2020.110287

23. S. Bai, S. Chen, Y. Zhao, T. Guo, R. Luo, D. Li, A. Chen, Gas sensing properties of Cd-doped ZnO nanofibers synthesized by the electrospinning method. J. Mater. Chem. A **2**(39), 16697–16706 (2014). https://doi.org/10.1039/C4TA03665D

24. U. Chaitra, A.V.M. Ali, A.E. Viegas, D. Kekuda, K.M. Rao, Growth and characterization of undoped and aluminium doped zinc oxide thin films for $SO_2$ gas sensing below threshold value limit. Appl. Surf. Sci. **496**, 143724 (2019). https://doi.org/10.1016/j.apsusc.2019.143724

25. J. Ding, J. Zhu, P. Yao, J. Li, H. Bi, X. Wang, Synthesis of ZnO–Ag hybrids and their gas-sensing performance toward ethanol. Ind. Eng. Chem. Res. **54**(36), 8947–8953 (2015). https://doi.org/10.1021/acs.iecr.5b01711

26. B. Hartiti, M. Siadat, E. Comini, M.M. Hashitha, M. Arachchige, S. Fadili, P. Thevenin, Acetone sensor based on Ni doped ZnO nanostructues: growth and sensing capability. J Mater Sci Mater. Electron. **30**(8), 7681–7690 (2019). https://doi.org/10.1007/s10854-019-01083-9

27. B.G. Shohany, L. iMotevalizadeh, M. E. Abrishami, Investigation of ZnO thin-film sensing properties for $CO_2$ detection: effect of Mn doping. J Theor Appl Phys. **12**(3), 219–225 (2018). https://doi.org/10.1007/s40094-018-0302-3

28. E. Naik, H.S.B. Indrajith, R. Naik, B.R. Viswanath, M.C. Kirthan, Prabhakara, Effect of zirconium doping on the structural, optical, electrochemical and antibacterial properties of ZnO nanoparticles prepared by sol-gel method. Chem. Data Collect. (2020). https://doi.org/10.1016/j.cdc.2020.100505

29. V. Gokulakrishnan, S. Parthiban, K. Jeganathan, K. Ramamurth, Investigation on the effect of Zr doping in ZnO thin films by spray pyrolysis. Appl. Surf. Sci. **257**(21), 9068–9072 (2011). https://doi.org/10.1016/j.apsusc.2011.05.102

30. U. Demirkol, S. Pat, R. Mohammadigharehbagh, C. Musaoğlu, M. Özgür, S. Elmas, S. Özen, Ş Korkmaz, Investigation of the substrate effect for Zr doped ZnO thin film deposition by thermionic vacuum arc technique. J Mater Sci: Mater Electron. **29**(21), 18098–18104 (2018). https://doi.org/10.1007/s10854-018-9920-4

31. M.A. Desai, V. Sharma, M. Prasad, S. Jadkar, G.D. Saratale, S.D. Sartale, Seed-layer-free deposition of well-oriented ZnO nanorods thin films by SILAR and their photoelectrochemical studies. Int. J. Hydrog. Energy **45**(10), 5783–5792 (2020). https://doi.org/10.1016/j.ijhydene.2019.09.150

32. S.S. Zahirullah, P. Immanuel, S. Pravinraj, P.F.H. Inbaraj, J.J. Prince, Synthesis and characterization of Bi doped ZnO thin films using SILAR method for ethanol sensor. Mater. Lett. **230**, 1–4 (2018). https://doi.org/10.1016/j.matlet.2018.07.067

33. A. Santhamoorthy, P. Srinivasan, A. Krishnakumar, J.B.B. Rayappan, K.J. Babu, SILAR-deposited nanostructured ZnO thin films: effect of deposition cycles on surface properties. Bull. Mater. Sci. **44**(3), 1–8 (2021). https://doi.org/10.1007/s12034-021-02465-8

34. S.D. Ponja, S. Sathasivam, I.P. Parkin, C.J. Carmalt, Highly conductive and transparent gallium doped zinc oxide thin films via chemical vapor deposition. Sci. Rep. **10**(1), 1–7 (2020). https://doi.org/10.1038/s41598-020-57532-7

35. K.D.A. Kumar, S. Valanarasu, J.S. Ponraj, B.J. Fernandes, M. Shkir, S. AlFaify, P. Murahari, K. Ramesh, Effect of Er doping on the ammonia sensing properties of ZnO thin films prepared by a nebulizer spray technique. J. Phys. Chem. Solids **144**, 109513 (2020). https://doi.org/10.1016/j.jpcs.2020.109513

36. K.D.A. Kumar, S. Valanarasu, A. Kathalingam, K. Jeyadheepan, $Nd^{3+}$ Doping effect on the optical and electrical properties of $SnO_2$ thin films prepared by nebulizer spray pyrolysis for opto-electronic application. Mater. Res. Bull. **101**, 264–271 (2018). https://doi.org/10.1016/j.materresbull.2018.01.050

37. V. Kumar, H. Sharma, S.K. Singh, S. Kumar, A. Vij, Enhanced near-band edge emission in pulsed laser deposited ZnO/c-sapphire nanocrystalline thin films. Appl. Phys. A **125**(3), 1–7 (2019). https://doi.org/10.1007/s00339-019-2485-0

38. D. Das, P. Mondal, Photoluminescence phenomena prevailing in c-axis oriented intrinsic ZnO thin films prepared by RF magnetron sputtering. RSC Adv. **4**(67), 35735–35743 (2014). https://doi.org/10.1039/C4RA06063F

39. J. Ghosh, R. Ghosh, P.K. Giri, Tuning the visible photoluminescence in Al doped ZnO thin film and its application in label-free glucose detection. Sens. Actuators B Chem. **254**, 681–689 (2018). https://doi.org/10.1016/j.snb.2017.07.110

40. S. Pati, P. Banerji, S.B. Majumder, Properties of indium doped nanocrystalline ZnO thin films and their enhanced gas sensing performance. RSC Adv. **5**(75), 61230–61238 (2015). https://doi.org/10.1039/C5RA10919A

41. M.S.A. El-saddek, I.S. Yahia, Z.A. Alahmed, F. Yakuphanoglu, Photoluminescence and optical dispersion parameters of N-doped ZnO nano-fiber thin films. J Electroceram. **30**(3), 152–158 (2013). https://doi.org/10.1007/s10832-012-9777-5

42. T. Chelouche, F. Touam, D. Boudjouan, R. Djouadi, A. Mahiou, G. Bouloufa, Z.H. Chadeyron, Na doping effects on the structural, conduction type and optical properties of sol–gel ZnO thin films. J Mater Sci. Mater. Electron. **28**(2), 1546–1554 (2017). https://doi.org/10.1007/s10854-016-5694-8

43. K. Ravichandran, A. Manivasaham, K. Subha, A. Chandrabose, R. Mariappan, Cost-effective nebulizer sprayed ZnO thin films for enhanced ammonia gas sensing-effect of deposition temperature. Surf. Interfaces **1**, 13–20 (2016). https://doi.org/10.1016/j.surfin.2016.06.004

44. V.G. Krishnan, P. Elango, Influence of Ba doping concentration on the physical properties and gas sensing performance of ZnO nanocrystalline films: automated nebulizer spray pyrolysis (ANSP) method. Optik **141**, 83–89 (2017). https://doi.org/10.1016/j.ijleo.2017.05.045

45. A. Manivasaham, K. Ravichandran, K. Subha, Light intensity effects on the sensitivity of ZnO: Cr gas sensor. Surf. Eng. **33**(11), 866–876 (2017). https://doi.org/10.1080/02670844.2017.1331724

46. K.R. Devi, G. Selvan, M. Karunakaran, K. Kasirajan, L.B. Chandrasekar, M. Shkir, S. AlFaify, SILAR-coated Mg-doped ZnO thin films for ammonia vapor sensing applications. J. Mater. Sci. Mater. Electron. **31**, 10186–10195 (2020). https://doi.org/10.1007/s10854-020-03564-8

47. K. Ravichandran, A.J. Santhosam, M. Sridharan, Effect of tungsten doping on the ammonia vapour sensing ability of ZnO thin films prepared by a cost effective simplified spray technique. Surf. Interfaces **18**, 100412 (2020). https://doi.org/10.1016/j.surfin.2019.100412

48. G.H. Mhlongo, D.E. Motaung, F.R. Cummings, H.C. Swart, S.S. Ray, A highly responsive NH$_3$ sensor based on Pd-loaded ZnO nanoparticles prepared via a chemical precipitation approach. Sci. Rep. **9**(1), 1–18 (2019). https://doi.org/10.1038/s41598-019-46247-z

49. Z. Wang, Z. Tian, D. Han, F. Gu, Highly sensitive and selective ethanol sensor fabricated with In-doped 3DOM ZnO. ACS Appl. Mater. Interfaces **8**(8), 5466–5474 (2016). https://doi.org/10.1021/acsami.6b00339

50. Z. Li, J. Yi, Drastically enhanced ammonia sensing of Pt/ZnO ordered porous ultra-thin films. Sens. Actuators B: Chem **317**, 128217 (2020). https://doi.org/10.1016/j.snb.2020.128217